



**HAL**  
open science

# A Computational Study of a Two-fluid Atomizing Coaxial Jet: Validation against Experimental Back-lit Imaging and Radiography and the Influence of Gas Velocity and Contact Line Model

Lam Vu, Nathanaël Machicoane, Danyu Li, Timothy Morgan, Theodore Heindel, Alberto Aliseda, Olivier Desjardins

## ► To cite this version:

Lam Vu, Nathanaël Machicoane, Danyu Li, Timothy Morgan, Theodore Heindel, et al.. A Computational Study of a Two-fluid Atomizing Coaxial Jet: Validation against Experimental Back-lit Imaging and Radiography and the Influence of Gas Velocity and Contact Line Model. *International Journal of Multiphase Flow*, 2023, 10.1016/j.ijmultiphaseflow.2023.104520 . hal-04112632

**HAL Id: hal-04112632**

**<https://hal.science/hal-04112632>**

Submitted on 31 May 2023

**HAL** is a multi-disciplinary open access archive for the deposit and dissemination of scientific research documents, whether they are published or not. The documents may come from teaching and research institutions in France or abroad, or from public or private research centers.

L'archive ouverte pluridisciplinaire **HAL**, est destinée au dépôt et à la diffusion de documents scientifiques de niveau recherche, publiés ou non, émanant des établissements d'enseignement et de recherche français ou étrangers, des laboratoires publics ou privés.

# A Computational Study of a Two-fluid Atomizing Coaxial Jet: Validation against Experimental Back-lit Imaging and Radiography and the Influence of Gas Velocity and Contact Line Model

Lam Vu<sup>\*1</sup>, Nathanaël Machicoane<sup>2,4</sup>, Danyu Li<sup>3</sup>, Timothy B. Morgan<sup>3</sup>, Theodore J. Heindel<sup>3</sup>, Alberto Aliseda<sup>2</sup>, Olivier Desjardins<sup>1</sup>

<sup>1</sup>Department of Mechanical and Aerospace Engineering, Cornell University, Ithaca, USA

<sup>2</sup>Department of Mechanical Engineering, University of Washington, Seattle, USA

<sup>3</sup>Center for Multiphase Flow Research and Education and Department of Mechanical Engineering, Iowa State University, Ames, USA

<sup>4</sup>Univ. Grenoble Alpes, CNRS, Grenoble INP, LEGI, 38000 Grenoble, France

\*Corresponding author email: lxv2@cornell.edu

---

## Abstract

Numerical simulations of liquid atomization in a two-fluid coaxial geometry have been performed using a geometric Volume-of-Fluid method. Experimental measurements have been obtained using visible light back-lit imaging and X-ray radiography. Simulations are validated against experiments, using the same geometry and fluid injection rates of air and water, by showing excellent agreement in quantities such as liquid mass distribution in the spray formation region and the liquid jet length statistics and temporal dynamics. At the nozzle exit, the coflowing liquid and gas streams are separated by a cylindrical splitter plate. The liquid is laminar and modeled using a Poiseuille flow while the gas inflow model and the contact line model are varied. For the gas velocity models, the vorticity thickness is shown to have a strong influence on the downstream liquid distribution; the difficulty of its modeling and routes to overcome them are discussed. For the contact line model, pinning the interface to the inner wall of the splitter plate leads to an initial increase in the diameter of the liquid jet just downstream of the nozzle exit. In contrast, pinning to the outer wall of the splitter plate or allowing for a free moving contact line results in a monotonic decrease in the diameter of the liquid jet as the downstream distance is increased, in agreement with the experimental observations and measurements. A sub-grid scale contact line model based on a static contact angle is introduced. The static contact angle is varied in the model, showing that the liquid remains intact longer as the static contact angle is increased.

**Keywords:** Air-blast Atomization, Contact Line Modeling, Liquid-Gas Flows, Validation

---

## 1. Introduction

Two-fluid coaxial atomizers utilize a high-speed gas stream to destabilize a coflowing low-speed liquid jet. These devices are widely used in engineering systems such as spray dryers and fuel injectors. Accurate modeling of the liquid jet's initial destabilization and break up is of the utmost importance as it serves as an initial condition for the spray dispersion process. Because of the inherent difficulties associated with modeling primary atomization computationally [12], studies have mostly been limited to highly simplified and academic cases. Moreover, few studies have explored

19 in detail the modeling of the nozzle exit. In particular, the impact of different modeling strategies for the high-speed  
20 gas, low-speed liquid, and the splitter plate separating the two streams, warrants careful investigation.

21 Liquid atomization has been studied extensively both through experiments and simulations but have had limita-  
22 tions based on the methods used. A non-exhaustive list of such methods are described below along with some of  
23 their limitations. Experimentally, the flow inside the nozzle cannot be easily quantified using standard particle image  
24 velocimetry (PIV) and hot-wire measurements. Back-lit imaging is an effective technique for visualizing the spray  
25 and can be used to accurately extract quantitative measurements of the liquid presence in a region where the liquid  
26 stays mostly intact [20]. However, such measurements struggle in areas where the liquid is broken up and multiple  
27 liquid structures intersect a line of sight. In contrast, X-ray radiography penetrates the liquid, enabling the study of  
28 additional physics, such as bubble entrainment and contact line dynamics in extreme atomization conditions [21].  
29 Recently, it has been used to extract quantitative measurements such as the integrated liquid depth along a line of  
30 sight [3]. Simulations have had their own challenges such as robust numerical methods capable of handling topology  
31 change, discontinuous fluid properties across the interface and singular forces at the interface, and computational de-  
32 mand owing to the wide range of length and time scales [12]. Front tracking methods [37], which transport a surface  
33 mesh, are viable techniques but have difficulty with topology change as heuristics are needed for the deletion and  
34 re-population of surface elements. Diffuse interface methods [2] are also viable techniques, but diminish the sharp-  
35 ness of the discontinuities since the interface is smeared over a few computational cells. Level-set methods, which  
36 transport a signed distance function away from the interface, have been used extensively [35] but suffer from mass  
37 conservation issues. These issues have been addressed by improvements such as the conservative level-set method  
38 [5] and the refined grid level-set method [14]. Volume-of-Fluid (VOF) methods, using complex geometric transport  
39 operations [29], have had success in handling topology change, ensuring discrete mass conservation and maintaining  
40 the sharp discontinuities.

41 Validating simulations against experiments is a crucial step in computational studies of sprays and the majority  
42 of past validation exercises of two-fluid atomizers have compared indirect quantities or reduced the modeling com-  
43 plexity because of the computational and experimental challenges described above. Demoulin et al. [8] simulated  
44 primary break up by solving equations for a single fluid representing a liquid-gas mixture under the assumptions  
45 of high Reynolds and Weber numbers and compared centerline liquid volume fraction profiles against experiments.  
46 Gorokhovski et al. [12] modeled the primary atomization by solving for the gas phase using a large-eddy simulation  
47 (LES) and the liquid phase using a stochastic liquid depletion modeling. This study yielded satisfactory agreement  
48 of liquid volume fraction distributions against experiments but most comparisons were qualitative. Fuster et al. [11]  
49 presented simulations in a planar configuration at a lower viscosity and density ratio and compared droplet size dis-  
50 tributions, as a function of mesh size, against experimental data. Fuster et al. [10] studied the influence of the splitter  
51 plate thickness on the peak frequency and made comparisons against linear stability analysis at low density ratios. For  
52 a single case, the frequency was compared against experiments and linear stability analysis at air-water conditions.  
53 The study showed that at low gas-to-liquid dynamic pressure ratios, a convective instability is observed whereas at

54 high dynamic pressure ratios, the instability is absolute. Xiao et al. [39] simulated primary atomization at air-water  
55 conditions and showed great agreement in the average liquid core length, where the liquid core is defined to be the  
56 large coherent liquid structure attached to the nozzle, but generated the gas inflow using synthetic turbulence. This  
57 study showed the turbulent eddies in the liquid phase play a leading role on the interfacial instabilities. Muller et al.  
58 [28] simulated primary break up of a high-viscosity fluid and showed excellent agreement in liquid core length and  
59 dominant frequency against experiments using the same geometry. Agbaglah et al. [1] presented 3D simulations in a  
60 planar geometry at experimental air-water conditions and compared well the liquid cone length and the most unstable  
61 frequency. This study showed that inclining the gas inflow enhanced the formation of interfacial waves. Ling et al.  
62 [19] performed massively resolved simulations at a lower density and viscosity ratio and reported on droplet size  
63 distributions, as a function of mesh size, and compared them against log-normal and Gamma distribution fits. The  
64 simulations qualitatively discussed the expansion of punctured holes in liquid sheets and the ligaments generated at  
65 the edge of their rims. Carmona et al. [4] performed simulations of a pre-filmed air-blast atomizer and made qualita-  
66 tive comparisons and drop size comparisons as a function of VOF iso-surface value. Even with current studies, more  
67 detailed and direct comparisons under realistic configurations are needed to validate computational capabilities.

68 In this work, we perform simulations of primary atomization in a coaxial two-fluid atomizer using the Volume-  
69 of-Fluid method and validate them against experiments. A novelty of our validation exercise is that we make direct  
70 comparisons of quantities obtained from experimental back-lit imaging and X-ray radiography under identical oper-  
71 ating conditions, using the same geometry. Furthermore, the validation is comprehensive, including comparisons of  
72 liquid mass distribution and temporal dynamics of the liquid jet. Following the validation, we study the effect of using  
73 different gas inflow models which range from using an analytical velocity profile to a nozzle simulation. The liquid  
74 is laminar and modeled as a Poiseuille flow and a cylindrical splitter plate separates the liquid and gas streams. We  
75 discuss the influence of the contact line model which ranges from pinning the interface to a specified location on the  
76 splitter plate (fixed triple point) to a free moving contact line. For free moving contact lines, we employ a sub-grid  
77 scale (SGS) contact line model that assumes a static contact angle [38]. We vary the static contact angle to understand  
78 the effect of nozzle tip wettability. These inflow modeling strategies are easily implementable and do not require large  
79 amounts of mesh resolution, making them particularly desirable from a practical engineering standpoint.

80 The paper is organized as follows: Section 2 discusses the experimental and numerical methods used, Section 3  
81 validates our computational model against experiment, Section 4 discusses the influence of the gas velocity model,  
82 Section 5 discusses the influence of the contact line model, and conclusions are drawn in Section 6.

## 83 **2. Methods**

### 84 *2.1. A Canonical Atomizer and Flow Conditions*

85 Figure 1 shows the two-fluid coaxial atomizer [21] used in both simulations and experiment. Air enters the  
86 nozzle through four upstream ports perpendicular to the wall and flows through an annular passage at a total flow

87 rate  $Q_g$ . Liquid water flows through a straight circular pipe at a flow rate  $Q_l$ . The outer wall of the liquid nozzle  
 88 separates the two streams and its annular section at the exit plane, with inner and outer nominal diameter  $d_l = 2$   
 89 mm and  $D_l = 3$  mm, will be referred to as the splitter plate. The liquid and gas bulk exit velocities are defined as  
 90  $U_l = Q_l/A_l$  and  $U_g = Q_g/A_g$ , where  $A_l = \pi d_l^2/4$  and  $A_g = \pi(d_g^2 - D_l^2)/4$  are the liquid and gas nozzle exit flow-  
 91 through areas and  $d_g = 10$  mm is the gas nozzle inner diameter. The fluid properties used are kinematic viscosities of  
 92  $\nu_g = 1.45 \times 10^{-5} \text{ m}^2 \text{ s}^{-1}$  and  $\nu_l = 1.137 \times 10^{-6} \text{ m}^2 \text{ s}^{-1}$ , densities of  $\rho_g = 1.226 \text{ kg m}^{-3}$  and  $\rho_l = 1000 \text{ kg m}^{-3}$ , and  
 93 a surface tension coefficient  $\sigma = 72 \text{ mN m}^{-1}$  where subscripts  $g$  and  $l$  denote gas and liquid properties respectively.  
 94 Table 1 summarizes the non-dimensional parameters used in this case.

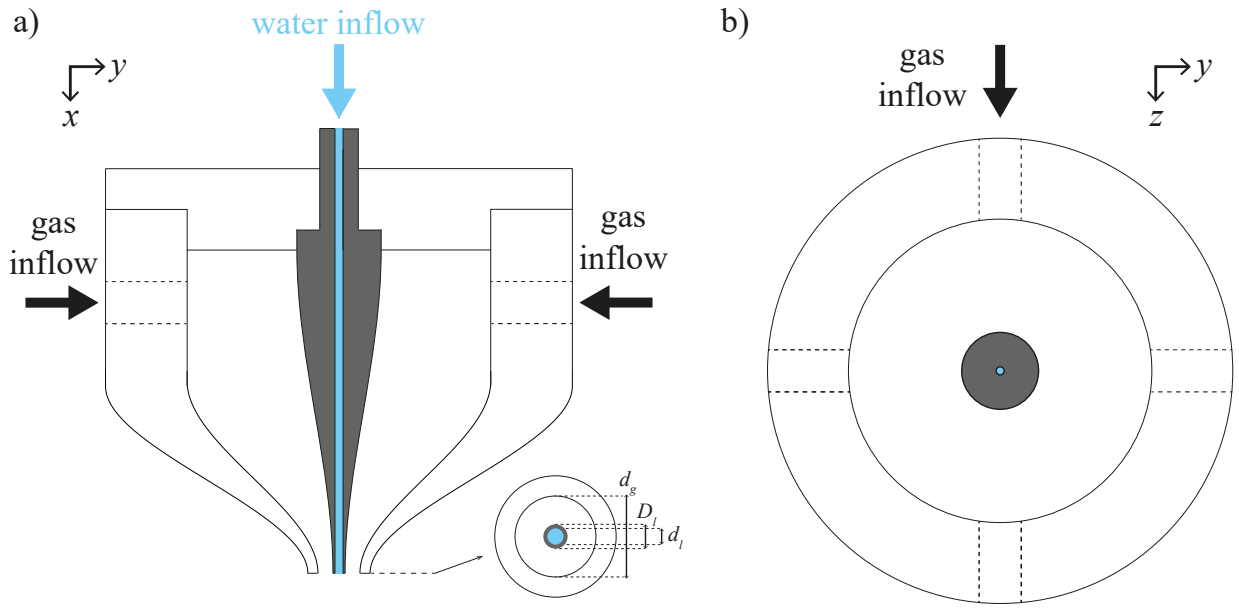


Figure 1: (Color online) Nozzle schematic cut longitudinally (left) and transversely (right). Water is injected through a round pipe while gas is injected through four gas ports into a converging nozzle. Note that the inset indicating the exit diameters in a) has been scaled up by a factor of two for visibility.

Table 1: Simulation's non-dimensional parameters: gas Reynolds number ( $Re_g$ ), liquid Reynolds number ( $Re_l$ ), gas-to-liquid dynamic pressure ratio ( $M$ ), Weber number based on the liquid jet diameter but gas density and slip velocity between the two phases ( $We$ ), density ratio ( $\rho^*$ ) and viscosity ratio ( $\mu^*$ ).

$Re_g \equiv \frac{4Q_g}{\sqrt{4\pi A_g \nu_g}}$	$Re_l \equiv \frac{\rho_l U_l d_l}{\mu_l}$	$M \equiv \frac{\rho_g U_g^2}{\rho_l U_l^2}$	$We \equiv \frac{\rho_g (U_g - U_l)^2 d_l}{\sigma}$	$\rho^* \equiv \frac{\rho_l}{\rho_g}$	$\mu^* \equiv \frac{\mu_l}{\mu_g}$
21400	1200	6.4	39.1	815	65

## 95 2.2. High-speed Back-lit Imaging and X-ray Radiography

96 High-speed back-lit imaging is used to produce 2D projections of the liquid presence in the near-field. The images  
 97 are post-processed using a sequence of operations that binarize the liquid core, defined to be the portion of the liquid

98 jet that is still fully connected to the nozzle, such that a liquid pixel value is 1 and a gas pixel value is 0. The temporal  
 99 and spatial resolutions for this study are 0.1 ms and 27  $\mu\text{m}$  respectively. Details of this method are discussed further  
 100 in [20].

101 Synchrotron X-ray radiography of the resulting spray was performed at the Advance Photon Source (APS) at  
 102 Argonne National Laboratory, 7-BM beamline [17]. As opposed to binarized liquid data obtained from back-lit  
 103 imaging, focused-beam radiography enables the point-wise measurement of the integrated liquid depth along a line of  
 104 sight, referred to as the equivalent path length (EPL). The measurement technique relies on a monochromatic X-ray  
 105 beam that is sent through the liquid and measured by a receiving pin-diode at 270 kHz. Based on the attenuation of  
 106 the signal caused by the liquid, the *EPL* is deduced from Beer-Lambert's Law:  $EPL = (1/\mu_a)\ln(I_0/I)$  where  $I_0$  is  
 107 the incident beam intensity,  $I$  is the beam intensity after passing through the spray, and  $\mu_a$  is the X-ray attenuation  
 108 coefficient of water at the X-ray wavelength. These point measurements can be raster-scanned across the spray to  
 109 gather longitudinal or transverse profiles of the liquid depth. Details of this technique are further described in [3, 13],  
 110 and the experimental configurations and liquid phase visualization are detailed in [21].

### 111 2.3.

112 We consider an LES approach to the two-phase, incompressible Navier-Stokes equations

$$113 \quad \nabla \cdot \tilde{\mathbf{u}} = 0, \quad (1)$$

$$114 \quad \frac{\partial \rho \tilde{\mathbf{u}}}{\partial t} + \nabla \cdot (\rho \tilde{\mathbf{u}} \tilde{\mathbf{u}}) = -\nabla \tilde{p} + \rho \mathbf{g} + \nabla \cdot (\mu [\nabla \tilde{\mathbf{u}} + \nabla \tilde{\mathbf{u}}^T]) + \nabla \cdot \boldsymbol{\tau}_{SGS} + \mathbf{F}_{ST}, \quad (2)$$

116 where  $\tilde{(\cdot)}$  denotes a spatially filtered (resolved) quantity on the mesh,  $\mathbf{u}$  is the velocity,  $p$  is the pressure,  $\rho$  is the  
 117 density,  $\mu$  is the dynamic viscosity,  $\mathbf{g}$  is the gravitational acceleration,  $\boldsymbol{\tau}_{SGS}$  is the sub-grid scale (SGS) stress,  $\mathbf{F}_{ST}$  is  
 118 the surface tension force and  $t$  is time. We also consider the volume fraction transport equation

$$119 \quad \frac{\partial \tilde{\alpha}}{\partial t} + \tilde{\mathbf{u}} \cdot \nabla \tilde{\alpha} = 0, \quad (3)$$

where  $\alpha$  is the ratio of liquid volume to cell volume in a computational cell and sub-grid scale effects have been  
 neglected. The fluid properties are weighted based on the liquid volume fraction

$$\rho = (1 - \tilde{\alpha})\rho_g + \tilde{\alpha}\rho_l, \quad (4)$$

$$\mu^{-1} = (1 - \tilde{\alpha})\mu_g^{-1} + \tilde{\alpha}\mu_l^{-1}, \quad (5)$$

120 where subscripts 'g' and 'l' refer to gas and liquid quantities respectively.

121 The two-phase Navier-Stokes equations are solved using an in-house, conservative, finite-volume flow solver for  
 122 low Mach number flows [9]. The solver employs second-order accurate methods in time and space. Away from the  
 123 interface, the flow solver is discretely kinetic energy conserving. At the interface, local discontinuities degrade the  
 124 methods and although mass is still discretely conserved and momentum is approximately conserved, kinetic energy

125 conservation is lost. The volume fraction equation is solved with a geometric, semi-Lagrangian Volume-of-Fluid  
 126 method [29]. Inside each computational cell, the interface is represented locally as a plane using the piece-wise linear  
 127 interface construction (PLIC) [33], with the plane normal calculated using LVIRA [30]. A dynamic Smagorinsky  
 128 turbulence model [27] is used to close  $\tau_{SGS}$ . The surface tension force is calculated through

$$129 \quad \mathbf{F}_{ST} = \sigma(\tilde{\kappa} + \kappa_{SGS})\nabla\tilde{\alpha} \quad (6)$$

130 where  $\sigma$  is the surface tension coefficient,  $\tilde{\kappa}$  is the resolved curvature and  $\kappa_{SGS}$  is a sub-grid scale curvature. The  
 131 surface tension force is embedded as a source term in the pressure Poisson equation using a continuous surface force  
 132 approach [31]. The resolved curvature of the interface is calculated using parabolic surface fits [34].  $\kappa_{SGS}$  is used to  
 133 model surface wettability effects that exist at scales far below the mesh size and is controlled through a static contact  
 134 angle  $\theta_s$  (see [38]). Figure 2 shows a schematic of a grid cell that contains the triple point. In that cell, the mismatch  
 135 between the interface angle resolved by the mesh ( $\theta_d$ ) and the angle at the wall ( $\theta_s$ ) is used to compute a SGS curvature

$$136 \quad \kappa_{SGS} = \frac{\cos\theta_s - \cos\theta_d}{\Delta}, \quad (7)$$

137 where  $\Delta$  is the mesh spacing. If a cell does not have a triple point, then  $\kappa_{SGS}$  is set to 0.

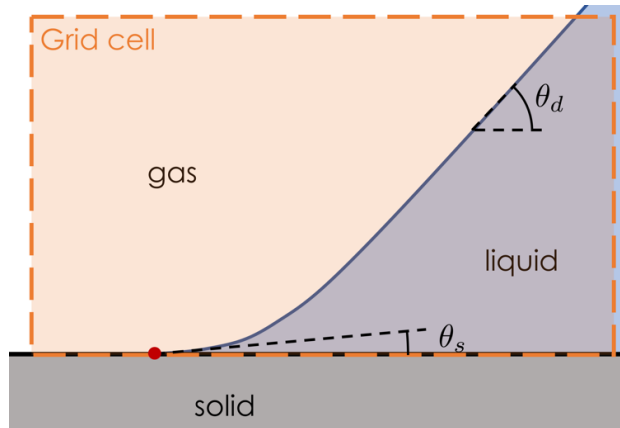


Figure 2: (Color online) Schematic of sub-grid scale contact line. The model adds a sub-grid scale curvature based on an assumed static contact angle  $\theta_s$  to the resolved curvature based on  $\theta_d$ .

## 138 2.4. Simulation Set Up

### 139 2.4.1. Domain

140 The atomization domain is a rectangular box of size  $11.16D_l \times 10D_l \times 10D_l$ , discretized on a Cartesian mesh  
 141 uniformly spaced by  $n_x \times n_y \times n_z$  cells. Cells are cubic with sides of length  $\Delta/d_l = 0.066$ .  $x$  is the downstream  
 142 direction while  $y$  and  $z$  are the lateral directions with the origin of the domain located at the center of the nozzle exit  
 143 plane. The liquid is laminar and given a parabolic velocity profile. The gas inflow condition is either specified by a

144 Dirichlet condition according to an analytical profile or a supplementary nozzle simulation. All other boundaries are  
145 treated as Neumann outflow conditions.

146 For some of the atomization simulations presented herein, an auxiliary nozzle simulation of the internal gas flow  
147 of the nozzle is used to generate realistic inflow conditions. The domain size of this nozzle simulation is  $10d_g \times$   
148  $10d_g \times 10d_g$  and the mesh is Cartesian with a uniform spacing  $\Delta_n/d_g = 0.05$ . The gas nozzle simulation is indicated  
149 in terms of the gas diameter  $d_g$  since it is the relevant quantity here, and we remind that  $D_l/d_g = 0.3$ . The nozzle  
150 plenum is the furthest point upstream in the domain and the furthest point downstream is at a distance  $d_g$  past the  
151 nozzle exit. The liquid injection is masked out as a solid and a single-phase solver is used, significantly reducing  
152 the computational cost. The converging nozzle walls are created by stair-stepping full cells that are treated as solid  
153 boundaries and the gas inflow is injected through the four normal ports upstream to match the gas flow rate  $Q_g$ . This  
154 approach matches the nozzle 3D geometry used in the experiment and available at <http://depts.washington.edu/fluidlab/nozzle.shtml>. All other boundaries are treated as Neumann outflow conditions. The gas velocity  
155 field at  $x = -1.16D_l$  is then used as a Dirichlet inflow condition for the atomization simulation.  
156

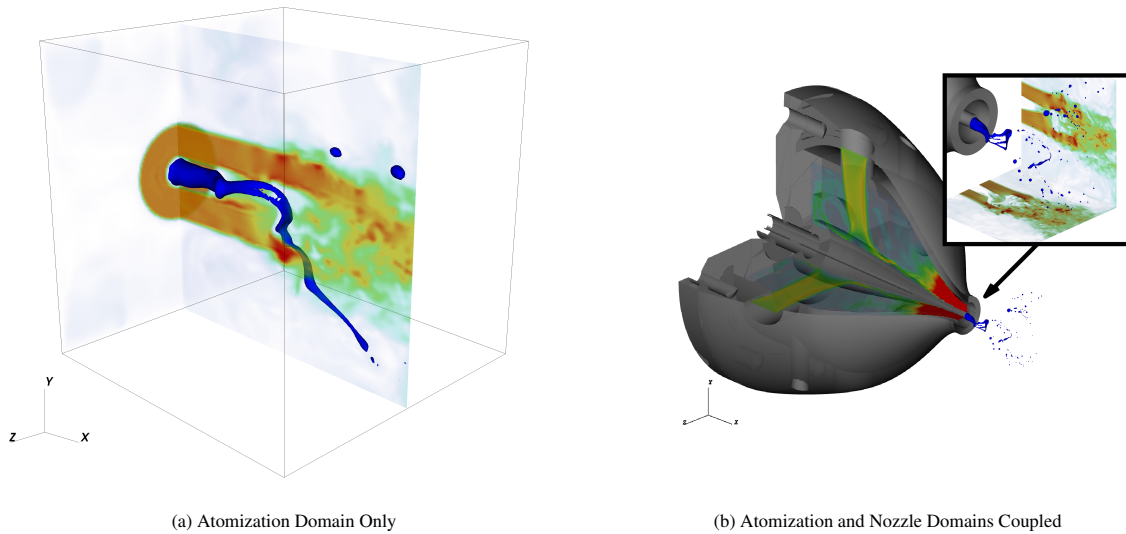


Figure 3: (Color online) Illustration of the computational set up. Contour of  $\alpha = 0.5$  representing the interface is plotted in blue, pseudo-color of velocity magnitude are plotted on the cut planes with different normalization inside and outside the nozzle. a) Domain excludes the nozzle and utilizes an analytical profile to model the gas velocity and b) a separate nozzle simulation is coupled to the atomization domain.



157 *2.4.2. Range of Gas Velocity and Contact Line Models*

158 The gas velocity models used in this study were an analytical velocity profile and an additional nozzle simulation  
 159 of the internal gas flow. The analytical profile [24] and takes the form

$$\begin{aligned}
 u(r) &= U_g \operatorname{erf}((r - R_l)/\delta_w) [1 + \operatorname{erf}((r - R_l)/\delta_w)]/2 & R_l \leq r \leq r_g \\
 v(r) &= w(r) = 0
 \end{aligned}
 \tag{8}$$

161 where  $R_l = D_l/2$  and  $r_g = d_g/2$  are the lower and upper bounds containing the gas stream,  $r$  is the radial location,  
 162  $\delta_w$  is the prescribed gas vorticity thickness and  $U_g$  is chosen such that the gas volumetric flow rate integrates to  $Q_g$ .  
 163 Figure 3a shows an atomization simulation run with an analytical gas velocity profile while Fig. 3b shows a simulation  
 164 where the nozzle and atomization simulations are coupled as described in Section 2.4.1.

165 The contact line models used in this study were pinning the contact line to the inner wall ( $r = r_l = d_l/2$ ) pinning  
 166 to the outer wall ( $r = R_l$ ) and allowing for an unpinned/free moving contact line. The implementation of each is as  
 167 follows: when pinning to  $r_l$ , the splitter plate is modeled as a fully unwet wall while when pinning to  $R_l$ , it is modeled  
 168 as a fully wet wall. In both cases, the splitter plate cells are treated as a solid boundary for the velocity solver, but  
 169 either taken to be a full liquid or gas cells when included in the LVIRA interface reconstruction. However, in the case  
 170 where the contact line is free moving, the splitter plate cells are excluded from the LVIRA interface reconstruction but  
 171 still treated as a solid boundary for velocity. For freely moving contact lines, the SGS contact line model described in  
 172 Section 2.3 is employed. It should be noted that although the splitter plate is resolved by 2-3 cells in this study, results  
 173 presented in the following section show that excellent agreement with experiment is still obtained. More detailed  
 174 analysis of the contact line in a more highly resolved setting is left for future work.

175 **3. Validation Against Experiments**

176 The combination of using an additional nozzle simulation to model the gas profile and allowing for a free contact  
 177 line with a static contact angle of  $85^\circ$  yields the best agreement against experiments; qualitative comparisons are made  
 178 in Fig. 4 and quantitative comparisons are made against metrics gathered from X-ray measurements in Fig. 5 and from  
 179 back-lit imaging in Fig. 6. The atomization simulation presented in this section uses a refined mesh of size  $\Delta/2$ .

180 Figure 4 shows snapshots of the flow comparing the simulations and experiments; emphasis is placed on the  
 181 liquid core. At this low gas-to-liquid dynamic pressure ratio, the main instabilities observed are Kelvin-Helmholtz  
 182 instabilities that develop just past the nozzle exit and a large-scale flapping instability. At large-scales, both exhibit  
 183 similar liquid core lengths, interface topology, and flapping motion. The three snapshots illustrate the small-scale  
 184 event of bag break up. The process begins with the development of a thick sheet, the high-speed gas subsequently  
 185 inflates this sheet which forms a bag, and finally, when the sheet becomes sufficiently thin, the bag bursts. These thin  
 186 sheets in the experiment can reach scales as small as  $O(1 \mu\text{m})$  which computations cannot afford to resolve. In our  
 187 simulations, the mesh sizes are  $O(100 \mu\text{m})$  and as such, bags prematurely break and leave behind large rims resembling  
 188 a prong. Running at these mesh sizes allow simulations to be relatively affordable, costing around 100,000 core hours.

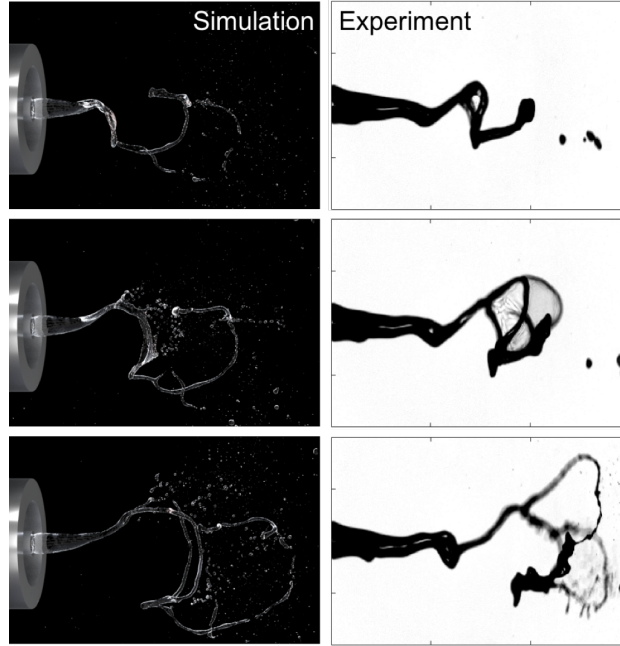


Figure 4: (Color online) Qualitative comparisons between the simulation (left) and experiment (right). Frames are separated by 1 ms.

189 Quantitative comparisons of EPL statistics, liquid core length, and dominant frequency are presented to validate  
 190 simulations against experiments. EPL is calculated in the simulation by integrating the liquid volume fraction along a  
 191 line of sight, i.e.,  $EPL = \int \alpha dz$ . After the flow has reached a statistically stationary state, statistics are accumulated for  
 192  $T_{stat} = 113d_l/U_l = 450$  ms, i.e., 113 characteristic liquid time scales, while experimental measurements are gathered  
 193 for 10 seconds, corresponding to 45 and 1000 flapping events respectively. Figure 5a shows a 2D map of EPL averaged  
 194 in time. Figure 5b shows the comparison of mean EPL sampled along  $x$ , at the centerline ( $y = 0$ ). The mean centerline  
 195 EPL is a proxy for the liquid diameter at distances close to the nozzle exit and decreases in value downstream either  
 196 because the flapping instability displaces the liquid core transversely away from the line of sight or the liquid core  
 197 has deformed or fragmented. *EPL* measurements presented herein are normalized by  $D_l$  since we will later pin the  
 198 contact line to the outer wall of the liquid pipe, leading to a value of approximately 1 at the nozzle exit,  $x/D_l = 0$   
 199 (Note: it will not be exactly 1 because of the inexact nature associated with approximating a cylindrical geometry  
 200 using a Cartesian mesh). Simulations are in excellent agreement with experiments as they are able to match well  
 201 the centerline decay of mean EPL. Figure 5c shows that the simulations also match well the experimental standard  
 202 deviation (std) of centerline EPL. Peaks in the standard deviation of EPL occur where variations in the integrated  
 203 volume fraction over time are largest and in the case of the centerline EPL, are visually confirmed to be a result  
 204 of large-scale flapping motion. Figures 5d to 5k show excellent agreement in transverse EPL mean and standard  
 205 deviation profiles. Figures 5d to 5g show that the simulations matches the transverse mean profiles well, capturing the  
 206 spreading of the liquid jet. Figure 5h shows two peaks in the standard deviation transverse profile at the top and bottom

207 edges of the jet and can be explained by the variation in volume fraction caused by interfacial perturbations generated  
 208 by Kelvin-Helmholtz instabilities [23, 32]. Figures 5i to 5k show that as the downstream distance is increased, the  
 209 centerline value and the two off-center peaks also increase, indicating a transition from a surface Kelvin-Helmholtz  
 210 instability to a large-scale flapping instability.

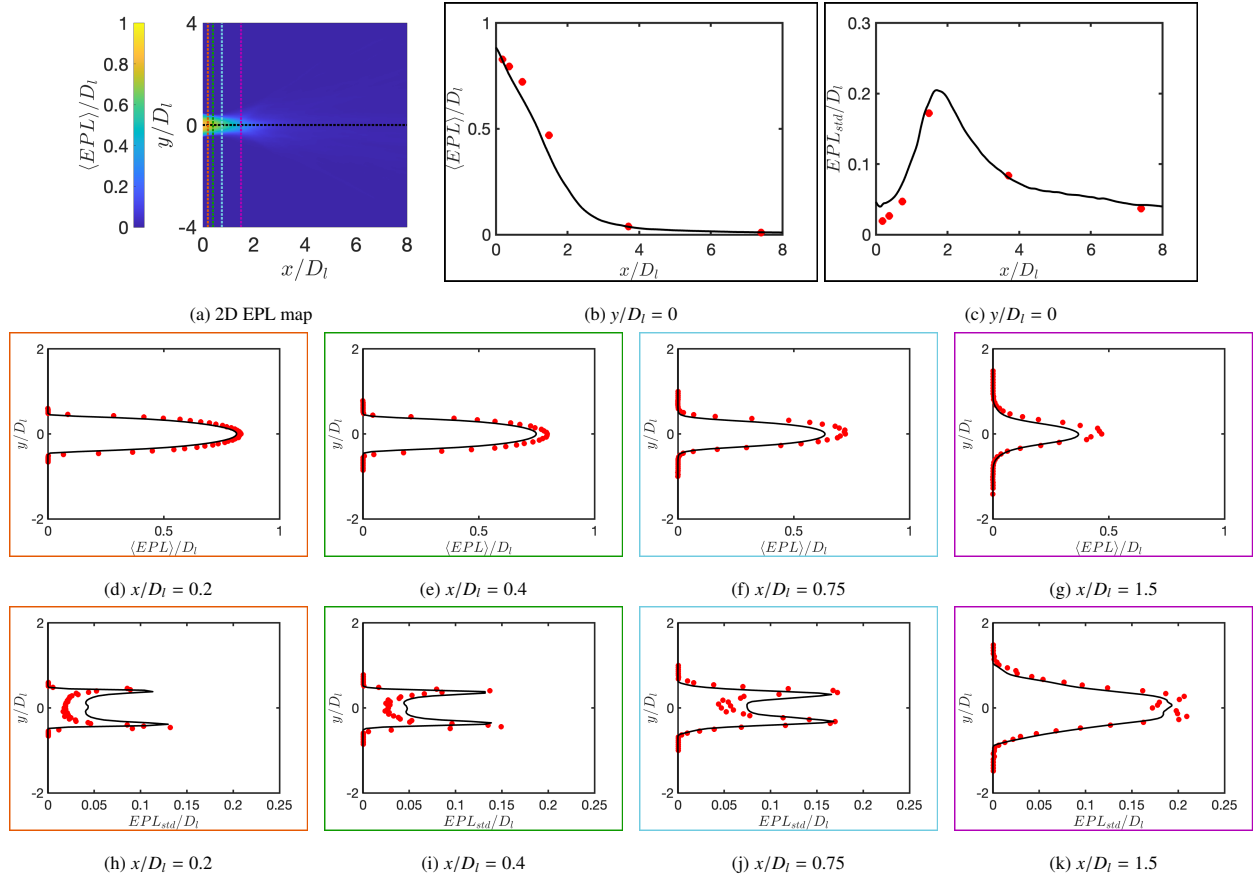


Figure 5: (Color online) Simulations compared against experiments. a) 2D mean EPL map with sampling locations marked, b-k) Transverse profiles of the mean (middle row) and standard deviation (bottom row) EPL, comparing the simulation (—) and the experimental measurements (●).

211 Figure 6a shows a time instance of a binarized image of the liquid core and mimics an experimental back-lit image.  
 212 The quantities illustrated on the figure are the liquid core length  $L_B$ , defined to be the instantaneous longitudinal  
 213 extent of the liquid core, and the  $y$  liquid presence barycenter ( $y_{bary}$ ) at a downstream location. Figure 6b shows  
 214 that the simulations agree well with experimental results for the normalized probability density functions (PDF) of  
 215  $L_B$ . Figure 6c shows a spectrum of a Fourier transform taken of a time signal of  $y_{bary}$  (see [16] for more details). A  
 216 flapping Strouhal number is calculated through  $St = f_{dom} d_l / U_g$  where  $f_{dom}$  is the dominant frequency taken to be the  
 217 frequency at which the spectrum peaks.  $y_{bary} \approx x/D_l = 3$ ,  $x/D_l$  [7]. Note that this normalization does not claim any  
 218 physical scaling but is done for non-dimensionalization purposes. Table 2 summarizes the comparison of the mean

219 and standard deviation of  $L_B$  and the flapping Strouhal number between the simulations and the experiments.

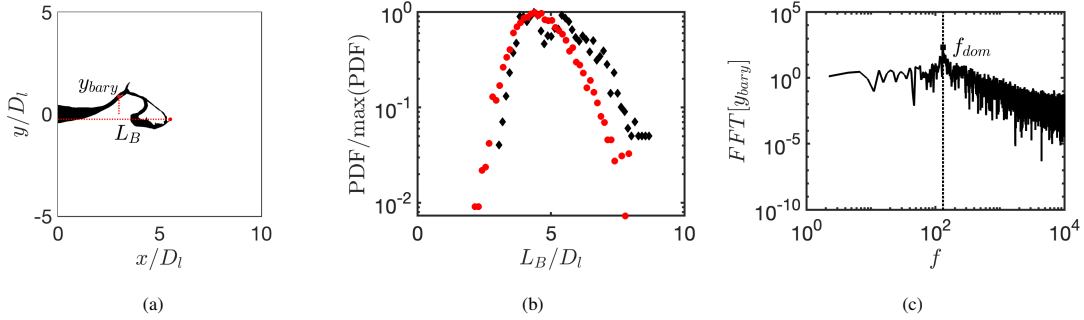


Figure 6: (Color online) a) Simulation binarized image of the liquid core with relevant quantities, b) PDF of liquid core length comparing the simulation ( $\blacklozenge$ ) and the experiment ( $\bullet$ ), and c)  $y$   $x/D_l = 3$ ,  $f_{dom}$ .

Table 2: Comparisons between the simulation and the experiment of mean and standard deviation of  $L_B$  and flapping Strouhal number obtained from binarized images.

	$\langle L_B \rangle / D_l$	$L_{B, std} / D_l$	$St$
Simulation	5.24	1.15	$7.52 \times 10^{-3}$
Experiment	4.67	0.937	$6.63 \times 10^{-3}$
Normalized Difference	12%	22%	13%

220 We now look at the effect of mesh resolution on the statistics presented above. Two additional simulations using  
 221 larger mesh resolutions  $\Delta$  and  $2\Delta$  are presented. Figure 7 shows the mean and standard deviation centerline EPL  
 222 statistics and the PDF of liquid core length at these different mesh sizes. Mean and standard deviation centerline EPL  
 223 statistics indicate that a simulation with a mesh resolution  $\Delta$  is relatively well converged because differences between  
 224  $\Delta$  and  $\Delta/2$  are small compared to differences between  $2\Delta$  and  $\Delta$ . Furthermore, Fig. 7c shows that the liquid core length  
 225 is not strongly affected by the mesh size. Although discrepancies are still present in statistics between mesh sizes  
 226  $\Delta$  and  $\Delta/2$ , we conclude that a mesh size  $\Delta$  is sufficient to draw inferences from. As such, to reduce computational  
 227 resources, future simulations presented will maintain a mesh size of  $\Delta$ .

## 228 4. Impact of Gas Velocity Model

### 229 4.1. Gas Velocity Profiles

230 Figure 8 shows velocity profiles at the nozzle exit plane for the experiment, the auxiliary nozzle simulation and  
 231 the analytical velocity profiles according to Eq. (8) at different vorticity thicknesses. For the analytical profiles, the  
 232 vorticity thicknesses used are  $2\delta_w$ ,  $\delta_w$  and  $\delta_w/2$  where  $\delta_w = 5.6h / \sqrt{Re_h}$  is the vorticity thickness obtained from the  
 233 correlation proposed by [23],  $h = (D_l - d_g)/2$  and  $Re_h = U_g h / \nu_g$ . No turbulent fluctuations are added to the inflow

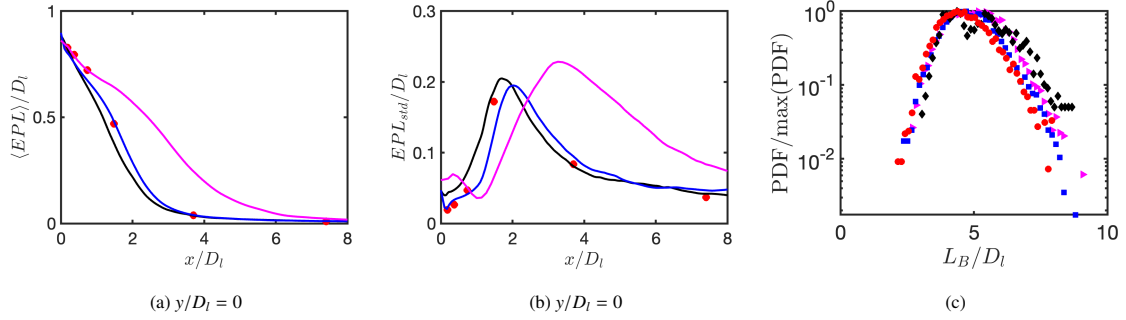


Figure 7: (Color online) Mesh convergence of a-b) EPL statistics and c) liquid core length PDFs for simulations with mesh sizes  $2\Delta$  (—,  $\blacktriangleright$ ),  $\Delta$  (—,  $\blacksquare$ ),  $\Delta/2$  (—,  $\blacklozenge$ ) compared against experiment ( $\bullet$ ).

234 velocity profile. The experimental gas velocity profiles were measured a small distance downstream of the nozzle  
 235 using hot-wires without any liquid present while the statistics in the simulation were sampled in the atomization  
 236 domain. Various mesh sizes of the auxiliary nozzle simulation were tested and minimal changes in the stream-wise  
 237 velocity statistics were observed. Figure 8a shows that the mean stream-wise velocity profile of the nozzle simulation  
 238 and the analytical velocity profile with  $\delta_w/2$  match the experimental vorticity thickness at the inner wall while the  
 239 velocity profiles with vorticity thicknesses of  $\delta_w$  and  $2\delta_w$  are a worse match. Figure 8b shows that the stream-wise  
 240 standard deviation velocity predicted from the nozzle simulation match the experiment well at the inner wall, which  
 241 can be expected to be most relevant for atomization, but are under-predicted within the outer gas shear layer.

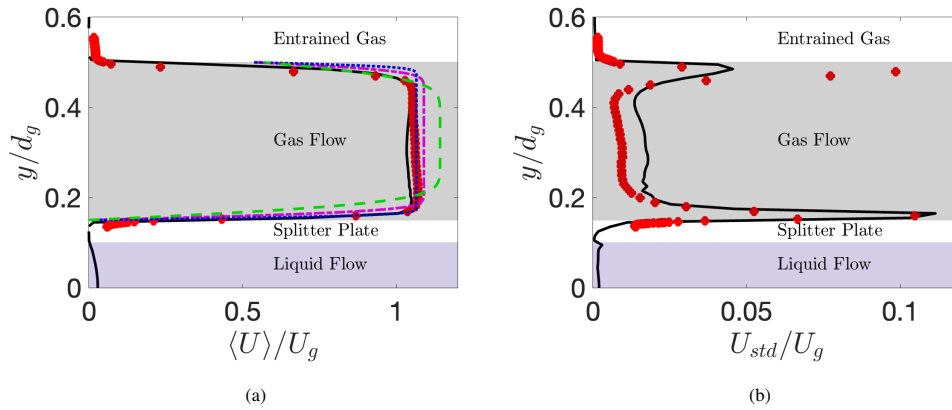


Figure 8: (Color online) Comparisons of velocity statistics between analytical profiles with vorticity thicknesses  $2\delta_w$  (— $\square$ —),  $\delta_w$  (— $\square$ —),  $\delta_w/2$  (— $\square$ —), additional nozzle simulation (—) and experiment ( $\bullet$ ). Note that  $D_l/d_g = 0.3$ .

#### 242 4.2. Influence of Vorticity Thickness

243 Figures 9a and 9b show the mean and standard deviation centerline EPL and Fig. 9c shows the liquid core length  
 244 PDF of simulations using an analytical velocity profile at three different gas vorticity thicknesses (i.e.,  $2\delta_w$ ,  $\delta_w$  and  
 245  $\delta_w/2$ ). The contact line model used in these simulations was a free contact line with a static contact angle  $85^\circ$ . The

246 simulation presented in Section 3 using a mesh size  $\Delta/2$  will serve as a benchmark. Considering the simulation using  
 247 a gas vorticity thickness  $\delta_w$ , the mean centerline EPL profile and liquid core length PDF have larger values compared  
 248 to the benchmark case, suggesting that the jet breaks further downstream than in that case. Reducing the vorticity  
 249 thickness by a factor of 2 more closely matches the vorticity thickness produced from the nozzle simulation used  
 250 in the benchmark case and therefore, we observe better agreement in the mean centerline EPL profile. However,  
 251 discrepancies still remain as the standard deviation centerline EPL for  $x/D_l > 3$  and the liquid core length PDF  
 252 exhibits larger values. This can likely be attributed to the turbulence coming from the nozzle which is known to have a  
 253 destabilizing effect [15] and absent in the analytical inflow velocity profiles. Mean centerline EPL statistics and liquid  
 254 core length for  $2\delta_w$  have much larger values than all cases, confirming that increasing vorticity thickness increases the  
 255 liquid core length. Table 3 summarizes the mean and standard deviation liquid core length and the flapping Strouhal  
 256 number. Results show that decreasing the vorticity thickness decreases the mean liquid core length while increasing  
 257 the dominant frequency. The latter is a trend consistent with past studies [10, 24] and related to studying the influence  
 258 of gas velocity deficits on temporal dynamics [24, 25]. However, using an analytical profile seems to under-predict  
 259 the flapping Strouhal number by approximately 30% under the range of vorticity thicknesses presented here. This is  
 260 further evidence that turbulent fluctuations play a key role on the break up processes and in particular, on the dominant  
 261 frequencies [15, 26].

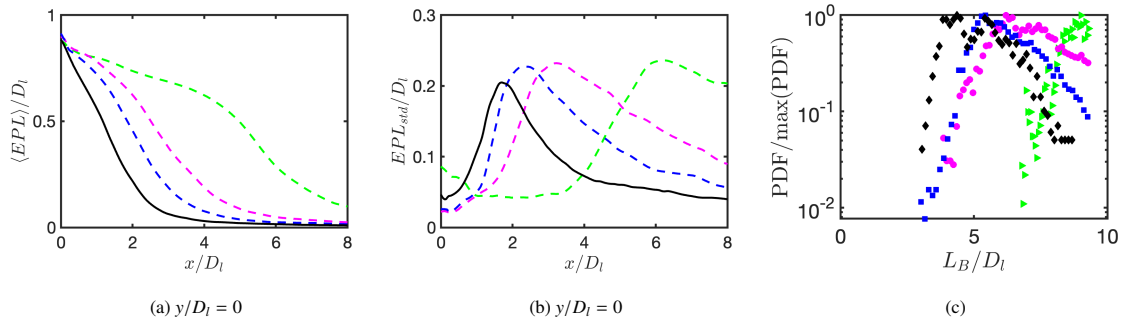


Figure 9: (Color online) Influence of velocity model on a-b) EPL statistics and c)  $2\delta_w$  (—,  $\blacktriangleright$ ),  $\delta_w$  (—,  $\bullet$ ) and  $\delta_w/2$  (—,  $\blacksquare$ ) compared against the benchmark (—,  $\blacklozenge$ ).

Table 3: Summary of mean and standard deviation of  $L_B$  and flapping Strouhal number obtained from binarized images for gas velocity profiles at different vorticity thicknesses.

	$\langle L_B \rangle / D_l$	$L_{B, std} / D_l$	$St$
$2\delta_w$	8.59	0.539	$4.66 \times 10^{-3}$
$\delta_w$	6.92	1.18	$4.93 \times 10^{-3}$
$\delta_w/2$	6.24	1.16	$5.57 \times 10^{-3}$
Benchmark	5.24	1.15	$7.52 \times 10^{-3}$

## 262 5. Impact of Contact Line Model

### 263 5.1. Effect of Contact Line Location

264 The contact line model was varied by pinning the contact line to the splitter plate inner wall, outer wall and  
 265 allowing for a free moving contact line with a static contact angle of  $85^\circ$ . The gas flow model was maintained as an  
 266 analytical velocity profile according to Eq. (8) with a vorticity thickness  $\delta_w$ .

267 Pinning the interface to the inner wall models the splitter plate as a fully unwet wall. This contact line model  
 268 creates a gas re-circulation and low pressure region just downstream of the splitter plate. This gives rise to aspiration  
 269 of the interface in the radial direction towards the gas. The consequence of this is observed in Fig. 10a where the  
 270 initial mean EPL increases as the downstream distance is increased. It is only after  $x/D_l \approx 0.25$ , that the interface  
 271 reaches the bulk of the high-speed gas stream and subsequently exhibits a monotonic decrease in mean EPL.

272 Pinning the interface to the outer wall models the splitter plate as a fully wet wall. Experimental high-resolution  
 273 visible light imaging and X-ray imaging have shown that at this operating condition, the contact line lies mostly near  
 274 the outer wall [13, 32]. Moreover, when adding swirl to the gas, it is observed that the contact line can even wick up  
 275 into the gas flow region as shown in Fig. 11a. Therefore, pinning to the outer wall more closely matches the local  
 276 experimental flow configuration. This pinning model results in a mean centerline EPL that decreases monotonically  
 277 which is experimentally observed (see Fig. 5b).

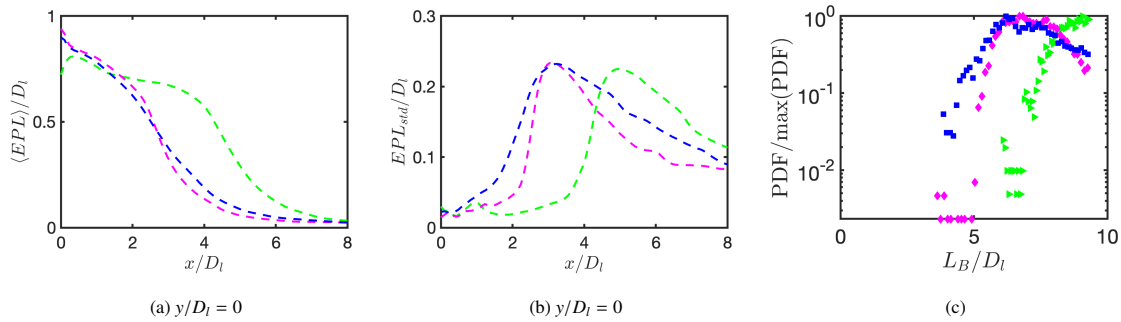


Figure 10: (Color online) Influence of contact line model on a-b) EPL statistics and c) liquid core length PDFs for pinned to inner wall (—,  $\blacktriangleright$ ), outer wall (—,  $\blacklozenge$ ) and a free contact line (—,  $\blacksquare$ ).

278 One can see in Fig. 10a that using a free contact line with an SGS contact line force with  $\theta_s = 85^\circ$  leads to similar  
 279 mean EPL profiles to pinning to the outer wall. Figure 11b shows the PDF of the normalized radial location for the  
 280 contact line such that a value of 0 indicates the interface is located at the inner wall while a value of 1 indicates it is  
 281 at the outer wall. For  $\theta_s = 85^\circ$ , the contact line radius peaks near the outer wall, serving as an explanation of why  
 282 pinning to the outer wall and this free contact line have similar mean EPL profiles. It can be observed in Fig. 10b that  
 283 a free contact line model leads to more interfacial dynamics than pinning the outer wall since its standard deviation  
 284 EPL profile is uniformly larger.

285 Figure 10c shows the PDF of the liquid core length and Table 4 summarizes the mean and standard deviation  
 286 centerline EPL and Strouhal numbers for all three cases. Pinning to the inner wall leads to a liquid that is too stable  
 287 as quantified by the large mean liquid core length and at times, the liquid core length is observed to exceed the  
 288 downstream domain boundary. Pinning to the outer wall and having a free contact line have similar PDFs, with the  
 289 free contact line exhibiting a slightly smaller mean liquid core length. Studies have shown that the vorticity thickness  
 290 has a strong impact on the dominant frequency [10, 24]. Results show that the flapping Strouhal numbers are all  
 291 within 2% of each other, suggesting that the dominant frequency is mostly independent of the contact line model for  
 292 a fixed vorticity thickness.

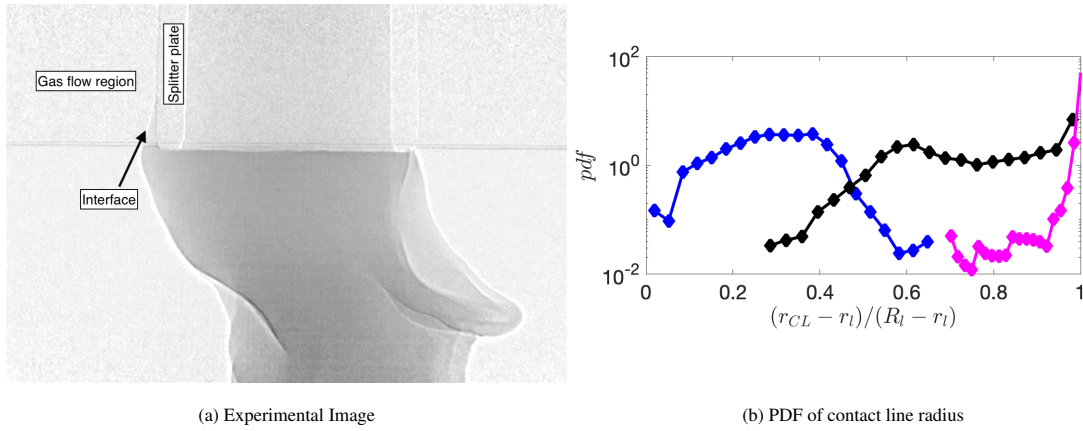


Figure 11: (Color online) a) Experimental image showing an instance where the contact line wicked up the outer wall into the gas flow region in the presence of gas swirl and b)  $\theta_s = 70^\circ$  (—),  $\theta_s = 85^\circ$  (—),  $\theta_s = 110^\circ$  (—).

Table 4: Summary of mean and standard deviation of  $L_B$  and flapping Strouhal number for different contact line models.

	$\langle L_B \rangle / D_l$	$L_{B, std} / D_l$	$St$
Pin to inner wall	8.50	0.583	$4.92 \times 10^{-3}$
Pin to outer wall	7.16	0.950	$5.06 \times 10^{-3}$
Free contact line	6.92	1.18	$4.92 \times 10^{-3}$

## 293 5.2. Effect of Static Contact Angle $\theta_s$

294 The static contact angle depends on many factors such as surface roughness, temperature, nozzle material and  
 295 treatment. For aluminum, water and air, a reasonable static contact angle is between  $70^\circ - 90^\circ$  [22, 40]. In the  
 296 present study, we consider the static contact angles  $70^\circ$ ,  $85^\circ$ , and  $110^\circ$  which model a moderately hydrophilic, less  
 297 hydrophilic, and moderately hydrophobic surface respectively. In these simulations, an auxiliary nozzle simulation  
 298 was used to provide the gas inflow velocity. Figure 11b shows the contact line radius PDFs measured at a fixed arc



299 location. The PDFs show that the contact lines sit very close to the outer wall for  $\theta_s = 70^\circ$ , further away from the  
 300 outer wall for  $\theta_s = 85^\circ$  and near the inner wall for  $\theta_s = 110^\circ$ . Figure 12a shows the mean and standard deviation  
 301 centerline EPL profiles for simulations using these static contact angles. Because a simulation using  $\theta_s = 110^\circ$  results  
 302 in a contact line close to the inner wall, its EPL profile follows a similar behavior to pinning to the inner wall, with an  
 303 initial increase in EPL and subsequent monotonic decrease. Similarly, a simulation using  $\theta_s = 70^\circ$  results in a contact  
 304 line close to the outer wall and as such, exhibits a behavior similar to pinning to the outer wall in that a monotonic  
 305 decrease in EPL is observed. Figure 12b shows that increasing  $\theta_s$  shifts the standard deviation centerline EPL to the  
 306 right. Figure 12c shows the PDFs of the liquid core length for simulations using  $\theta_s = 70^\circ$  and  $85^\circ$  are similar while  
 307  $110^\circ$  results in a profile shifted to the right. Table 5 summarizes the mean and standard deviation centerline EPL and  
 308 flapping Strouhal number showing that as  $\theta_s$  is increased, the liquid core length and dominant frequency also increase.  
 309 This highlights the significant impact that the contact angle model can have on the downstream liquid distribution.

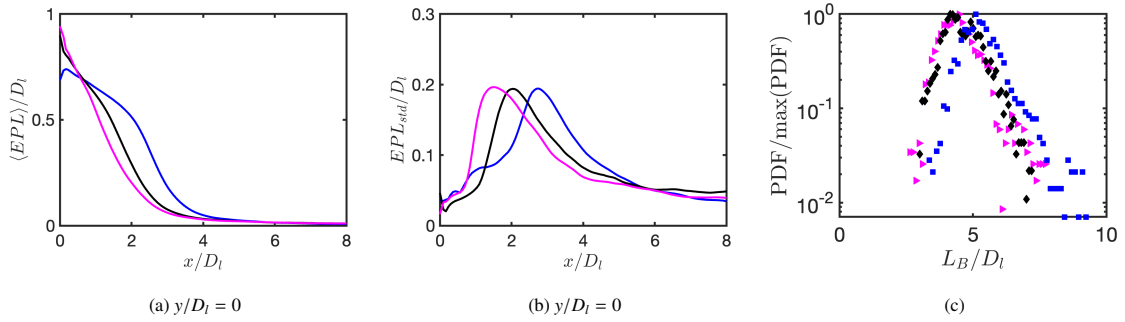


Figure 12: (Color online) Influence of static contact angle on a-b) EPL statistics and c) liquid core length PDFs for  $\theta_s = 70^\circ$  (—, ▶),  $85^\circ$  (—, ◆), and  $110^\circ$  (—, ■).

Table 5: Summary of mean and standard deviation of  $L_B$  and flapping Strouhal number for different static contact angles.

$\theta_s$	$\langle L_B \rangle / D_t$	$L_{B, std} / D_t$	$St$
$70^\circ$	4.52	0.810	$7.01 \times 10^{-3}$
$85^\circ$	4.65	0.751	$6.63 \times 10^{-3}$
$110^\circ$	5.38	0.866	$8.56 \times 10^{-3}$

## 310 6. Conclusion

311 In this study, we have performed simulations of air-blast atomization in a coaxial two-fluid atomizer using a geo-  
 312 metric Volume-of-Fluid method. Simulations were validated against experiments under identical air/water conditions  
 313 and geometries. Excellent agreement of quantities such as the mean equivalent path length of the liquid (EPL), liquid  
 314 core length, and dominant frequency was observed. A mesh refinement study was also conducted showing that these

315 quantities were reasonably well mesh converged. The liquid was modeled using a Poiseuille flow while the gas inflow  
316 and contact line models were studied.

317 The gas inflow models considered were analytical velocity profiles at different vorticity thicknesses with no tur-  
318 bulent fluctuations added and an auxiliary nozzle simulation. Simulations using analytical velocity profiles were  
319 benchmarked against a simulation using the nozzle simulation. Results showed that decreasing the vorticity thickness  
320 decreased the mean liquid core length, the mean centerline EPL, and increased the dominant frequency of the liquid  
321 jet motions. While one analytical profile had a vorticity thickness that was close in value to the experiment and nozzle  
322 simulation, quantities such as the mean liquid core length remained larger. Furthermore, although decreasing the  
323 vorticity thickness increased the dominant frequency, a trend reported in other studies [10, 24], the dominant frequen-  
324 cies for the presented vorticity thicknesses yielded systematically lower values than the experiment. These results  
325 confirmed that turbulent fluctuations in the gas play an important role.

326 The contact line models considered were pinning to the inner wall of the splitter plate, the outer wall of the splitter  
327 plate, and allowing for a free contact line with a (SGS) contact line model using a static contact angle of  $85^\circ$ . This  
328 study showed that the contact line model has a key influence on the liquid jet development and on the liquid distribution  
329 downstream. In particular, pinning to the outer wall or using a free moving contact line yielded better experimental  
330 agreement of quantities such as mean and standard deviation centerline EPL and mean liquid core length than pinning  
331 to the inner wall. Pinning to the inner wall resulted in an initial increase in mean centerline EPL downstream of the  
332 nozzle because of a re-circulation region created by the gas. In contrast, pinning to the outer wall or having a free  
333 moving contact line resulted in the monotonic decrease in EPL observed in the experiment. Results also indicated  
334 that when using an analytical gas velocity profile with a fixed vorticity thickness, the contact line model does not have  
335 a significant impact on the dominant frequency. The static contact angle was varied between  $\theta_s = 70^\circ$ ,  $\theta_s = 85^\circ$ ,  
336 and  $\theta_s = 110^\circ$ . Results showed in the  $\theta_s = 70^\circ$  case, i.e., modeling a hydrophilic surface, the mean centerline EPL  
337 exhibited similar trends to pinning to the outer wall while in the  $\theta_s = 110^\circ$  case, i.e., modeling a hydrophobic surface,  
338 trends were similar to pinning to the inner wall.

339 As the near-field region has been validated in this study and a better understanding of the impact of the gas velocity  
340 and contact line models have been gained, several research questions remain open. Since computational tools now  
341 result in strong agreement of liquid distribution compared against experiment, our research efforts will now shift  
342 to modeling the conversion of broken liquid structures in atomization simulations to Lagrangian particles in spray  
343 dispersion simulations. Promising research efforts have been made in this direction (e.g., [18, 36]) ([6]). The inflow  
344 modeling of the gas has been studied in various forms which include modeling the velocity profile just downstream  
345 of the nozzle exit using a velocity deficit (e.g., [24, 25]). However, current literature has not considered in detail the  
346 influence of the contact line which this study has shown to have an impact. Thus, a more detailed study of the contact  
347 line physics and different modeling strategies for the contact line would be useful.

348 **7. Acknowledgements**

349 This work was sponsored by the Office of Naval Research (ONR) as part of the Multidisciplinary University  
350 Research Initiatives (MURI) Program, under grant number N00014-16-1-2617. The views and conclusions contained  
351 herein are those of the authors only and should not be interpreted as representing those of ONR, the U.S. Navy or the  
352 U.S. Government.

353 The X-ray imaging work was performed at the 7-BM beamline of the Advanced Photon Source, a U.S. Depart-  
354 ment of Energy (DOE) Office of Science User Facility operated for the DOE Office of Science by Argonne National  
355 Laboratory under Contract No. DE-AC02-06CH11357.

356 **References**

- 357 [1] G Agbaglah, R. Chiodi, and O. Desjardins. Numerical simulation of the initial destabilization of an air-blasted liquid layer. *Journal of Fluid*  
358 *Mechanics*, 812:1024–1038, 2017.
- 359 [2] D. M. Anderson, G. B. McFadden, and A. A. Wheeler. Diffuse-interface methods in fluid mechanics. *Annual Review of Fluid Mechanics*,  
360 30(1):139–165, 1998.
- 361 [3] Julie K Bothell, Nathanael Machicoane, Danyu Li, Timothy B Morgan, Alberto Aliseda, Alan L Kastengren, and Theodore J Heindel.  
362 Comparison of X-ray and optical measurements in the near-field of an optically dense coaxial air-assisted atomizer. *International Journal of*  
363 *Multiphase Flow*, 125:103219, 2020.
- 364 [4] Julien Carmona, N. Odier, Olivier Desjardins, Benedicte Cuenot, A. Misdariis, and A. Cayre. A comparative study of direct numerical  
365 simulation and experimental results on a prefilming airblast atomization configuration. *Atomization and Sprays*, 31(8):9–32, 2021.
- 366 [5] R. Chiodi and O. Desjardins. A reformulation of the conservative level set reinitialization equation for accurate and robust simulation of  
367 complex multiphase flows. *Journal of Computational Physics*, 343:186–200, 2017.
- 368 [6] Robert Chiodi and Olivier Desjardins. General, robust, and efficient polyhedron intersection in the interface reconstruction library. *Journal*  
369 *of Computational Physics*, 449:110787, 2022.
- 370 [7] Antoine Delon, Alain Cartellier, and Jean-Philippe Matas. Flapping instability of a liquid jet. *Phys. Rev. Fluids*, 3:043901, Apr 2018.
- 371 [8] F. Demoulin, P. Beau, G. Blokkeel, A. Mura, and R. Borghi. A new model for turbulent flows with large density fluctuations: Application to  
372 liquid atomization. *Atomization and Sprays*, 17:315–345, 2007.
- 373 [9] O. Desjardins, G. Blanquart, G. Balarac, and H. Pitsch. High order conservative finite difference scheme for variable density low Mach  
374 number turbulent flows. *Journal of Computational Physics*, 227:7125–7159, 2008.
- 375 [10] D. Fuster, J.P. Matas, Marty S., Popinet S., J Hoepffner, Cartellier A., and Zaleski S. Instability regimes in the primary breakup region of  
376 planar coflowing sheets. *J. Fluid Mech.*, 736:150–176, 2013.
- 377 [11] Daniel Fuster, Anne Bagué, Thomas Boeck, Luis Le Moynes, Anthony Leboissetier, Stéphane Popinet, Pascal Ray, Rubenand Scardovelli,  
378 and Stéphane Zaleski. Simulation of primary atomization with an octree adaptive mesh refinement and VOF method. *International Journal*  
379 *of Multiphase Flow*, 35:550–565, 2009.
- 380 [12] M. Gorokhovski and M. Herrmann. Modeling primary atomization. *Annual Review of Fluid Mechanics*, 40:343–366, 2008.
- 381 [13] Theodore J. Heindel. X-ray imaging techniques to quantify spray characteristics in the near-field. *Atomization and Sprays*, 28:1029–1059,  
382 2018.
- 383 [14] M. Hermann. A balanced force refined level set grid method for two-phase flows on unstructured flow solver grids. *Journal of Computational*  
384 *Physics*, 227:2674–2706, 2008.
- 385 [15] D. Jiang and Y. Ling. Impact of inlet gas turbulence on the formation, development and breakup of interfacial waves in a two-phase mixing  
386 layer. *Journal of Fluid Mechanics*, 921:A15, 2021.
- 387 [16] Maxime Kaczmarek, Rodrigo Osuna-Orozco, Peter Dearborn Huck, Alberto Aliseda, and Nathanaël Machicoane. Spatial characterization of  
388 the flapping instability of a laminar liquid jet fragmented by a swirled gas co-flow. *International Journal of Multiphase Flow*, 152:104056,  
389 2022.
- 390 [17] Alan Kastengren, Christopher F. Powell, Dohn Arms, Eric M. Dufresne, Harold Gibson, and Jin Wang. The 7BM beamline at the aps: a  
391 facility for time-resolved fluid dynamics measurements. *Journal of Synchrotron Radiation*, 19(4):654–657, July 2012.
- 392 [18] Dokyun Kim and Parviz Moin. Subgrid-scale capillary breakup model for liquid jet atomization. *Combustion Science and Technology*,  
393 192:1334–1357, 2010.
- 394 [19] Y. Ling, D. Fuster, S. Zaleski, and G. Tryggvason. Spray formation in a quasi-planar gas-liquid mixing layer at moderate density ratios: A  
395 numerical closeup. *Phys. Rev. Fluids*, 2:014005, 2017.
- 396 [20] N. Machicoane, G. Ricard, R. Osuna-Orozco, P. Huck, and A. Aliseda. Influence of steady and oscillating swirl on the near-field spray  
397 characteristics in a two-fluid coaxial atomizer. *International Journal of Multiphase Flow*, 129:103318, 2020.
- 398 [21] Nathanael Machicoane, Julie K. Bothell, Danyu Li, Timothy B. Morgan, Theodore J. Heindel, Alan L. Kastengren, and Alberto Aliseda.

- 399        Synchrotron radiography characterization of the liquid core dynamics in a canonical two-fluid coaxial atomizer. *International Journal of*  
400        *Multiphase Flow*, 115:1–8, 2019.
- 401 [22] Majid H. Majeed. Static contact angle and large water droplet thickness measurements with the change of water temperature. *Al-Nahrain*  
402        *Journal for Engineering Sciences*, 17:114–128, 2014.
- 403 [23] Philippe Marmottant and Emmanuel Villermaux. On spray formation. *Journal of Fluid Mechanics*, 498:73–111, 2004.
- 404 [24] Jean-Philippe Matas, Antoine Delon, and Alain Cartellier. Shear instability of an axisymmetric air–water coaxial jet. *Journal of Fluid*  
405        *Mechanics*, 843:575–600, 2018.
- 406 [25] Jean-Philippe Matas, Sylvain Marty, and Alain Cartellier. Experimental and analytical study of the shear instability of a gas-liquid mixing  
407        layer. *Physics of Fluids*, 23(9):094112, 2011.
- 408 [26] Jean-Philippe Matas, Sylvain Marty, Mohamed Seydou Dem, and Alain Cartellier. Influence of gas turbulence on the instability of an air-water  
409        mixing layer. *Phys. Rev. Lett.*, 115:074501, August 2015.
- 410 [27] C. Meneveau, T. S. Lund, and W. H. Cabot. A Lagrangian dynamic subgrid-scale model of turbulence. *J. Fluid Mech.*, 319:353–385, 2000.
- 411 [28] T. Müller, A. Sänger, P. Habisreuther, T. Jakobs, D. Trimis, T. Kolb, and N. Zarzalis. Simulation of the primary breakup of a high-viscosity  
412        liquid jet by a coaxial annular gas flow. *International Journal of Multiphase Flow*, 87:212–228, 2016.
- 413 [29] M. Owkes and O. Desjardins. A computational framework for conservative, three-dimensional, unsplit, geometric transport with application  
414        to the volume-of-fluid (VOF) method. *Journal of Computational Physics*, 270:587–612, 2014.
- 415 [30] J. E. Pilliod and E. G. Puckett. Second-order accurate volume-of-fluid algorithms for tracking material interfaces. *Journal of Computational*  
416        *Physics*, 199:465–502, 2004.
- 417 [31] Stephane Popinet and Stephane Zaleski. A front-tracking algorithm for accurate representation of surface tension. *International Journal for*  
418        *Numerical Methods in Fluids*, 30:775–793, 1999.
- 419 [32] Guillaume Ricard, Nathanaël Machicoane, Rodrigo Osuna-Orozco, Peter D. Huck, and Alberto Aliseda. Role of convective acceleration in  
420        the interfacial instability of liquid-gas coaxial jets. *Phys. Rev. Fluids*, 6:084302, August 2021.
- 421 [33] William J. Rider and Douglas B. Kothe. Reconstructing volume tracking. *Journal of Computational Physics*, 141(2):112–152, 1998.
- 422 [34] Ruben Scardovelli and Stéphane Zaleski. Interface reconstruction with least-square fit and split Eulerian–Lagrangian advection. *International*  
423        *Journal for Numerical Methods in Fluids*, 41, 2003.
- 424 [35] J. A. Sethian and P. Smereka. Level set methods for fluid interfaces. *Annual Review of Fluid Mechanics*, 35(1):341–372, 2003.
- 425 [36] G. Tomar, D. Fuster, S. Zaleski, and S. Popinet. Multiscale simulations of primary atomization. *Computers & Fluids*, 39:1864–1874, 2010.
- 426 [37] G. Tryggvason, B. Bunner, A. Esmaeeli, D. Juric, N. Al-Rawahi, et al. A front-tracking method for the computations of multiphase flow.  
427        *Journal of Computational Physics*, 169(2):708–759, 2001.
- 428 [38] Sheng Wang and Olivier Desjardins. 3D numerical study of large-scale two-phase flows with contact lines and application to drop detachment  
429        from a horizontal fiber. *International Journal of Multiphase Flows*, 101:35–46, 2018.
- 430 [39] F. Xiao, M. Dianat, and J.J. McGuirk. LES of turbulent liquid jet primary breakup in turbulent coaxial air flow. *International Journal of*  
431        *Multiphase Flow*, 60:103–118, 2014.
- 432 [40] Zhi-Qiang Zhu, Yang Wang, Qiu-Sheng Liu, and Jing-Chang Xie. Influence of bond number on behaviors of liquid drops deposited onto  
433        solid substrates. *Microgravity Science and Technology*, 24, 06 2012.